### Title

Internal Biofilm Heterogeneities Enhance Solute Mixing and Chemical Reactions in Porous Media




### Journal

Environmental Science and Technology, 57(21)

### ISSN

0013-936X



### Authors

Markale, Ishaan

Carrel, Maxence

Kurz, Dorothee L

et al.



### Publication Date

2023-05-30

### DOI

10.1021/acs.est.2c09082

Peer reviewed

# Internal biofilm heterogeneities enhance solute mixing and chemical reactions in porous media

Ishaan Markale,[†,‡] Maxence Carrel,[¶] Dorothee L. Kurz,[‡,†] Verónica L. Morales,[§] Markus Holzner,[‖,†] and Joaquín Jiménez-Martínez[*,†,‡]

[†]*Eawag, Swiss Federal Institute of Aquatic Science and Technology, 8600 Dübendorf, Switzerland*

[‡]*Department of Civil, Environmental and Geomatic Engineering, ETH Zürich, 8093 Zürich, Switzerland*

[¶]*Geopraevent AG, 8045 Zürich, Switzerland*

[§]*Department of Civil and Environmental Engineering, University of California Davis, Davis, CA, USA 95616-5270*

[‖]*WSL, Swiss Federal Institute of Forest, Snow and Landscape Research, 8903 Birmensdorf, Switzerland*

E-mail: joaquin.jimenez@eawag.ch/jjimenez@ethz.ch

**Abstract**

Bacterial biofilms can form in porous media that are of interest in industrial applications ranging from medical implants to biofilters as well as in environmental applications such as in-situ groundwater remediation, where they can be critical locations for biogeochemical reactions. The presence of biofilms modifies porous media topology and hydrodynamics by clogging pores, and consequently solutes transport and reactions kinetics. The interplay between highly heterogeneous flow fields found in porous media and microbial behavior, including biofilm growth, results in a spatially heterogeneous

biofilm distribution in the porous media as well as internal heterogeneity across the thickness of the biofilm. Our study leverages highly resolved three-dimensional X-ray computed microtomography images of bacterial biofilms in a tubular reactor to numerically compute pore-scale fluid flow and solute transport by considering multiple equivalent stochastically generated internal permeability fields for the biofilm. We show that the internal heterogeneous permeability mainly impacts intermediate velocities when compared with homogeneous biofilm permeability. While the equivalent internal permeability fields of the biofilm do not impact fluid-fluid mixing, they significantly control a fast reaction. For biologically driven reactions such as nutrient or contaminant uptake by the biofilm, its internal permeability field controls the efficiency of the process. This study highlights the importance of considering the internal heterogeneity of biofilms to better predict reactivity in industrial and environmental bioclogged porous systems.

**Synopsis.** Internal heterogeneity of biofilms enhances fluid mixing and reactions, and biologically driven reactions, e.g., bio-accumulation, within porous media.

# 1 Introduction

Bacterial cells in open but also in confined systems such as porous media congregate embedding themselves in a self-made extra-polymeric matrix (extracellular polymeric substances, EPS), the so-called biofilm.[1,2] Biofilm formation can be problematic because of biofouling and corrosion in industrial systems.[3,4] However, biofilms can also be desirable in bioreactors,[5–7] wastewater treatment,[8] and bio-remediation of contaminated groundwater,[9,10] where biofilms, besides reducing the permeability,[11] act as hot spots for biogeochemical reactions. Therefore, there is a growing interest in understanding the development of biofilms in porous media systems and their properties in order to exercise optimal control on these processes.

The growth of biofilms in porous media alters the pore structure drastically.[11,12] This impacts hydrodynamics by creating preferential paths which cause flow channeling[13,14] and intermittency when the system approaches full clogging (i.e., the opening and closing of

individual preferential flow paths and their spatial rearrangement).[15,16] Biofilms have been demonstrated to have spatially and temporally varying physical (e.g., porosity[17,18]), rheological (e.g., shear strength[19]), and hydraulic (e.g., permeability[20]) properties. However, there is a significant challenge while trying to measure biofilm properties, and permeability in particular, due to the inability of most techniques to characterize biofilm structure without significantly affecting its properties.[21] A complete characterization of the fluid flow velocities within the biofilm is also challenging due to the inability of most tracer particles to penetrate the biofilm.[12,14,22] This has motivated the extensive use of numerical tools to characterize the entire velocity field within the biofilm-porous medium system.[23–27] However, most of the numerical approaches simulate fluid flow velocities assuming a constant permeability value for the biofilm, with varying orders of magnitude range.[23,24,26,27]

The formation of preferential paths and intermittency in the biofilm-porous medium system lead to anomalous or non-Fickian transport.[27–29] By creating regions of high and low fluid velocity, the physical heterogeneity controls the residence time of dissolved chemicals. Within the biofilm, many studies assume that diffusion is the primary mechanism controlling chemical transport (e.g., nutrient provision).[30–33] However, experimental works have shown that biofilms are permeable and have networks of submicroscopic channels,[34] where advective transport can take place.[22] To our knowledge, only a few studies have numerically investigated chemical transport in permeable biofilms within porous media.[23,27] Nevertheless, the impact of the internal complexity of the biofilm on fluid mixing and chemical reactions has not been addressed yet.

Stochastic simulations are often invoked in porous media research to model variable quantities such as porosity, permeability, and topological connectivity, at different scales, from field to pore scale.[35–37] Geostatistical simulations are used to generate multiple, equally probable representations of the spatial distribution of the attribute under study,[38] e.g., to model fracture networks.[39] Uncertainties are prevalent in natural and engineering systems at varying temporal and spatial scales, and they are modeled using these equally probable

representations. The potential of this approach to capture the internal complexity of the biofilm allocated within a porous medium, and therefore the spatial heterogeneity of physical properties (e.g., porosity and permeability), remains unexplored.

In this work, we resort to numerical simulations of modeling flow and solute transport within a bioclogged porous system. We use highly resolved three-dimensional X-ray computed images of a bioclogged porous medium to first construct randomized three-dimensional maps of biofilm permeability based on an underlying probability distribution function of permeabilities inferred from experimental imaging. We demonstrate the impact of this heterogeneous permeability field on pore-scale velocities, fluid mixing, and reactions. Finally, we also establish the relevance of considering the variability in biofilm internal properties when trying to predict the large-scale impact of biofilms on nutrient or contaminant uptake in a bioclogged porous medium. This can serve as a first step in modeling the impact of biofilm internal heterogeneity on the relevant industrial and environmental processes such as bio-accumulation and bio-remediation.

# 2 Materials and Methods

## 2.1 Biofilm geometry from X-ray imaging and tracer experiment

A tubular reactor of length 160 mm and diameter 10 mm was filled with Nafion grains of 2.5 mm diameter. The initial porosity of the reactor was $\sim 0.4$. A multi-species biofilm was grown for 7 days and fed using a solution of iron sulphate heptahydrate ($FeSO_4 \cdot 7H_2O$ at a concentration of 0.1 g/L) and glucose (at a concentration of 1 g/L). Iron sulphate ($FeSO_4$), a non-toxic inorganic compound, was added to the solution to act as contrast agent for the biofilm and was passively incorporated in the extra-polymeric matrix during its maturation. The experiment was conducted at a constant flowrate ($Q = 5\,\mathrm{mL/min}$). The experimental setup is shown in Figure 1. Three-dimensional (3D) images of the biofilm structures were obtained from a laboratory-based X-ray micro-Computed Tomography (micro-CT). A sec-

tion of the reactor (1/10) was imaged, from which the solid grains and the biofilm were reconstructed (Figure 2a and Supporting Information, Figure S1). We subsequently use this section for further analysis. For more details of biofilm culturing, the addition of contrast agent, and image acquisition, the reader is referred to Carrel et al. [40]

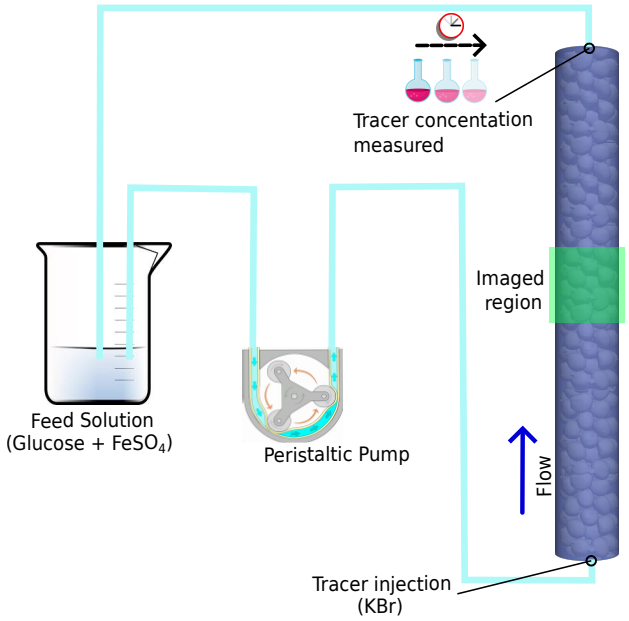


Figure 1: Schematic of the experimental setup used for growing and endpoint imaging of the biofilm by micro-CT. Feeding solution of glucose and iron sulphate heptahydrate ($FeSO_4 \cdot 7H_2O$) was used as contrast agent. Before and after the biofilm growth, a conservative tracer (potassium bromide, KBr) was injected at the inlet of the porous medium and its concentration was measured at the outlet of the domain to obtain breakthrough curves.

To characterize the impact of biofilm on solute transport, a tracer experiment before and after growing the biofilm was performed using potassium bromide (KBr). A pulse of tracer with concentration $c_{0,\mathrm{KBr}} = 0.303\,\mathrm{mol/m^3}$ was injected from the bottom (in the same flow direction as for growing the biofilm) at the same flow rate $Q$. Breakthrough curves (BTCs), i.e., the time series of the effluent concentration at the outlet (top), were obtained by collecting samples every 2 minutes and analyzing them with an atomic absorption spectrometer (Varian SpectrAA 220 FS).

## 2.2 Biofilm permeability field

The segmented 3D micro-CT images from the experiment (21 µm voxel resolution) provide binary fields of the spatial distribution of the biofilm and of the biofilm-free pore space. Different methods, e.g., the Turning-Band method[41] or the continuous and discrete spectral methods,[42,43] have been proposed to generate realizations of a field in 3D. Here, we use the Fast Fourier Transform Moving Average (FFT-MA) method[44,45] on the biofilm spatial grid to generate 3D statistically equivalent random permeability fields (see Supporting Information for details). The advantage of this method is that it generates the randomness in the permeabilities based on the spatial domain rather than the spectral domain, which allows us to relate the randomness to physical attributes of the biofilm such as the correlation length. A detailed discussion about this and other methods for generating random fields is out of the scope of this work and the reader is referred to Räss et al.[38] The underlying distribution of permeabilities is obtained from the experiments of Kurz et al.,[20] having mean $\mu_{\kappa_\mathrm{b}} = 5.12 \cdot 10^{-12}$ m$^2$ and variance $\sigma^2_{\kappa_\mathrm{b}} = 2.1716$ m$^4$ (i.e., a hydraulic heterogeneity of $\sigma^2_{\ln\kappa_\mathrm{b}} = 0.75$) (Figure 2b). Because of the high computational cost of our numerical model (Section 2.3), we use 10 different realizations and verified that the average and fluctuation do not change significantly with an increasing number of realizations. For the correlation length, we use the same as in this experimental data set $[\zeta_x, \zeta_y, \zeta_z] = [100, 100, 225]$ µm.[20] A sensitivity analysis to assess the impact of $\zeta_{x,y,z}$ on flow and transport has been carried out (see Supporting Information, Figure S2).

## 2.3 Numerical modeling

### 2.3.1 Fluid flow and transport modeling

The segmented three-dimensional images were imported into COMSOL Multiphysics®, a finite elements-based modeling program. It was used to solve for the flow and transport of a solute in the pore-space and within the biofilm. The flow in the porous space without biofilm

is governed by the incompressible steady-state Navier-Stokes equation and the continuity equation:

$$\rho(\boldsymbol{v}\cdot\nabla)\boldsymbol{v} = \nabla\cdot\left[-P\mathbf{I}+\mu(\nabla\boldsymbol{v}+(\nabla\boldsymbol{v})^T)\right] \tag{1a}$$

$$\nabla\cdot\boldsymbol{v} = 0 \tag{1b}$$

where $\rho$ is the liquid density (1000 kg/m$^3$), $\boldsymbol{v}$ is the velocity vector in three dimensions, $P$ is the pressure, $\mathbf{I}$ is the identity tensor and $\mu$ is the dynamic viscosity ($1\cdot10^{-3}$ kg/m s) of water. For the experimental flow rate ($Q = 5\,\mathrm{mL/min} = 8.333\cdot10^{-8}$ m$^3$/s) and empty porous medium, the resulting average pore-scale velocity is $\bar{v} = 2.65\,\mathrm{mm/s}$ and the Reynolds number $Re = 2.5$.

To solve the flow through the permeable biofilm in the bioclogged porous medium, we use the Brinkman equation,[46] which accounts for the transition from free to Darcy flow:

$$\frac{\rho}{n_\mathrm{b}}(\boldsymbol{v}\cdot\nabla)\boldsymbol{v}\frac{1}{n_\mathrm{b}} = \nabla\cdot\left[-P\mathbf{I}+\frac{\mu}{n_\mathrm{b}}\left(\nabla\boldsymbol{v}+(\nabla\boldsymbol{v})^T-\frac{2}{3}\frac{\mu}{n_\mathrm{b}}(\nabla\cdot\boldsymbol{v})\mathbf{I}\right)\right]-\left(\frac{\mu}{\kappa_\mathrm{b}}+\Phi\rho|\boldsymbol{v}|\right)\boldsymbol{v} \tag{2a}$$

$$\rho\nabla\cdot\boldsymbol{v} = 0 \tag{2b}$$

where $n_\mathrm{b}$ is the porosity of the biofilm matrix, $\kappa_\mathrm{b}$ is the biofilm permeability, and $\Phi = d_\mathrm{g}^2 n_\mathrm{b}^3/[150(1-n_\mathrm{b})^2]$ is the parameter in the Ergun equation.[47] The formulation of the Ergun equation is based on the consideration of the post-Darcy regime ($Re$ up to $\sim 10$), where the pressure drop is a function of the average velocity[48] and average solid grain diameter $d_\mathrm{g}$.

The transport of a chemical species in the empty pore space and within the biofilm is described by the advection-diffusion equation:

$$\frac{\partial c}{\partial t} + \nabla \cdot (\boldsymbol{v}c) - D\nabla^2 c = r \tag{3}$$

where $c$ is the concentration, $r$ is the reaction rate and $D$ is its molecular diffusion coefficient in water (here $10^{-9}\,\mathrm{m}^2/\mathrm{s}$). The transport is characterized by the dimensionless Péclet number, defined as the ratio between the characteristic time of diffusion ($t_D = \lambda^2/2D$) and the characteristic time of advection ($t_a = \lambda/\overline{v}$), $Pe = \bar{v}\lambda/2D \sim 1000$, where $\lambda = 1$ mm is the average pore length.

### 2.3.2 Particles recirculation for simulating the full reactor

Since the imaged geometry was 1/10 of the total length of the tubular reactor, and we want to compare our simulations to the transport experiments conducted for the full reactor, we simulate the advection of particles along streamlines of the flow field obtained from Equation 2a. Then, a recirculation protocol based on the reinjection of particles at the same velocity as they abandon the imaged domain (or their velocity before they get stuck at the solid-liquid interface due to their finite size) is used. The particles are reinjected 10 times, mimicking the total length of the reactor (see Supporting Information for details). We initially inject 10'000 particles at the inlet boundary (bottom), following a flux-weighted distribution of the velocities in the empty pore space as well as within the biofilm. Particle trajectories are computed in a Lagrangian reference frame with no diffusion. This simplification is acceptable because of the high $Pe$ used (tested for one realization). The particles are advected by the drag force given by $F_\mathrm{d} = (m_\mathrm{p}/\tau_\mathrm{p}) \cdot (v - v_\mathrm{p})$, where $m_\mathrm{p}$ is the mass of the particle, $\tau_\mathrm{p} = \rho_\mathrm{p} \cdot d_\mathrm{p}^2/18\mu$ is the velocity response time, with $d_\mathrm{p}$ being the particles diameter and $v_\mathrm{p}$ the particle velocity.[49]

### 2.3.3 Mixing, fluid-fluid reaction and chemical uptake by biofilm

In order to minimize the high computational cost of solving explicitly chemical reactions in the liquid phase, i.e., between an injected solution and the resident one, we compute the

mixing zone between both solutions and the reactivity within as follows. We initially inject as a pulse a chemical solution with an initial concentration $c_{0,\mathrm{m}} = 1\,\mathrm{mol/m^3}$, which corresponds to mass $m_{0,\mathrm{m}} = 1 \cdot 10^{-8}\,\mathrm{mol}$. The mixing zone $\Omega_\mathrm{m}$ (where $0 < c < 1$) is characterized by its volume, $V_\mathrm{m}\,[\mathrm{m^3}]$, defined in this case as $\Omega_\mathrm{m} = \{(x, y, z)|0.01 < c < 0.99\}$. We further assume that within this mixing zone a fast reversible reaction takes place, i.e., the characteristic reaction time scale ($t_r$) is smaller than the characteristic advective time (Damköhler number, $Da = t_a/t_r >> 1$). Then, the local reaction rate $r$ can be computed from the conservative concentration fields as follows:

$$r = \frac{2K}{(c^2 + 4K)^{3/2}} D||\nabla c||^2 \tag{4}$$

where $K$ is the equilibrium constant of the reaction (here $10^{-2}\,\mathrm{mol^2/m^6}$) and $||\,||$ denotes the magnitude of the concentration gradient vector.[50–52] The global reaction $R$, i.e., the upscaled reactivity, is computed as the integral of the local reaction rates $r$ over the mixing zone:

$$R = \int_{\Omega_\mathrm{m}} dx\,dy\,dz\,r \tag{5}$$

Previous studies have shown diffusion is typically the limiting mechanism for transporting chemicals within the biofilm.[31] Therefore, the bacteria composing the biofilm closer to the edge, i.e., closer to the preferential flow paths, take up more mass of chemicals than further from it, i.e., closer to the solid grains.[33,53] The rate at which chemicals are taken up can also be a complex function of the concentration.[54] Here, the chemicals advected and diffused through the biofilm are taken up following a linear relationship with concentration:

$$f(c) = k\,c \tag{6}$$

where $k$ is the rate coefficient (here 0.77 1/s).[33]

### 2.3.4 Model assumptions

To simplify the modeling in our study, we have made the following assumptions, which are common for such simulations. We assume that the presence of biofilm, and in particular the EPS, does not change the rheology of the liquid. We assume the biofilm is an immobile and non-deformable phase. Cell density and metabolic activity within the biofilm are considered spatially homogeneous. We also consider no-slip conditions at the fluid-solid interfaces. Considering a constant pressure gradient between the inlet and the outlet of the full reactor, constant pressure is set at the outlet of the imaged domain. The geometry was accurately resolved using a mesh of tetrahedral elements ($\sim 13 \cdot 10^6$ elements).

# 3 Results and Discussion

## 3.1 Biofilm permeability heterogeneity control on fluid flow velocities

Figure 2c shows a 3D rendering of a randomized realization of the internal biofilm permeability and the solid grains. The permeability values span over two orders of magnitude. The longer correlation length in the fluid flow direction ($\zeta_z$) can be recognized in the vertical orientation of high and low permeability regions within the biofilm. As it occurs in subsurface environments such as aquifers in unconsolidated sediments,[35] these elongated regions according to the main flow direction, and in particular the high permeability ones, are expected to play a key role in the internal connectivity within the biofilm. The advective transport and mass exchange within the biofilm are controlled by how the high permeability regions are connected.[22,34]

In the absence of bioclogging, the resulting flow field is relatively uniform (Figure 3a), albeit with higher velocities in pore bodies and lower velocities close to grains. Biofilm growth leads to the so-called double structure of the flow field.[55] A dual-porosity or dual-

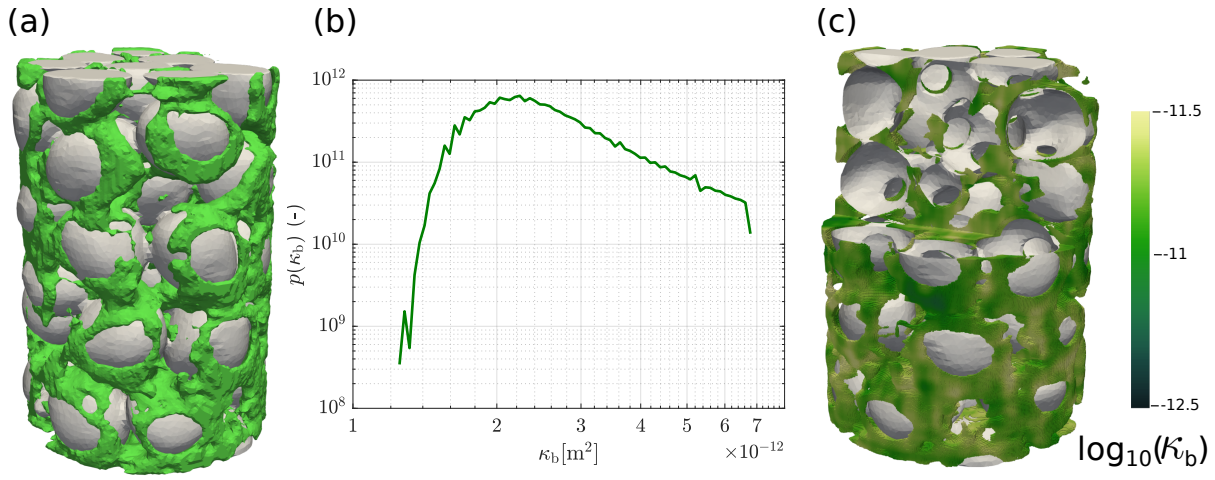


Figure 2: (a) Three-dimensional rendering of the biofilm (green color) and of the solid grains (gray color). (b) Underlying distribution of biofilm permeabilities ($\kappa_b$) from Kurz et al.[20] (c) A 3D randomized realization of the internal biofilm permeability and the surface of the solid grains (gray color) for visual clarity.

permeability system[13,56] arises with the presence of biofilm within the porous medium for a single-homogeneous value of biofilm permeability (Figure 3b). Figure 3c depicts a significant hydrodynamic change occurring when a heterogeneous permeability field is considered within the biofilm. A broader range of velocities can be found within the biofilm, with very low but also relatively high fluid flow velocities.

To further investigate the impact of biofilm and its internal permeability heterogeneity on the fluid flow velocities in the porous medium, we compute the probability density function of the fluid flow Eulerian velocities magnitude $v$, $p(v)$ (Figure 4a). When the porous medium is clean (black line), $p(v)$ shows a distribution observed in granular media that are well sorted.[14,55] However, when biofilm is considered impermeable (green line), the probability of both high and low velocities increases as physical heterogeneity increases, as previously observed for heterogeneous porous media[57] and in unsaturated conditions (e.g., in the presence of air).[58] Contrary to what is observed for heterogeneous and unsaturated porous media, where $p(v)$ for low velocities typically drop off algebraically following a power law ($p(v) \propto v^{\beta}$ with $\beta < 0$), a more complex behavior (i.e., changes in slope) is observed when permeable

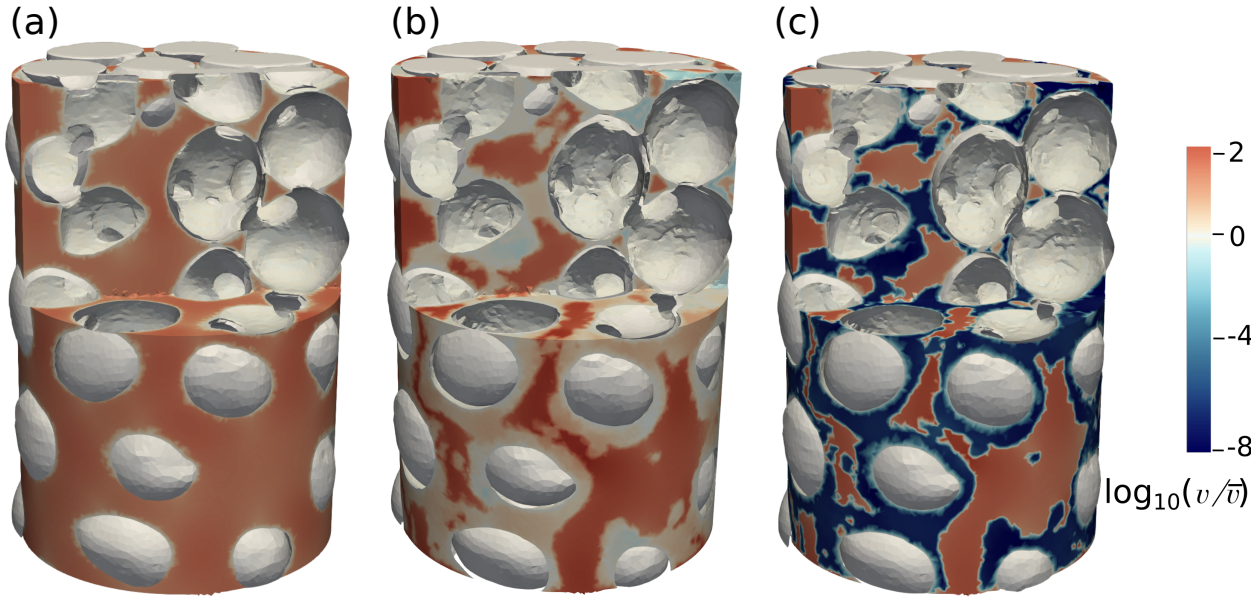


Figure 3: Fluid flow velocity field displayed in terms of the Eulerian velocity magnitude $v$ (same flow rate $Q = 8.333 \cdot 10^{-8}$ m$^3$/s) for (a) empty porous medium (i.e., without biofilm), (b) bioclogged porous medium with a single-homogeneous permeability value for the biofilm ($\kappa_b = 5.12 \cdot 10^{-12}$ m$^2$), and (c) bioclogged porous medium with a heterogeneous distribution of permeabilities within the biofilm ($\kappa_b \in [1.4, 7] \cdot 10^{-12}$ m$^2$). Grain surfaces (gray color) are shown for visual clarity.

biofilm (single-homogeneous value, $\kappa_b = 5.12 \cdot 10^{-12}$ m$^2$) is considered (yellow line). This is in agreement with previous findings for a permeable biofilm in 2D.[20,27] In the range of very low velocities, a similar scaling (i.e., $p(v) \sim v^{-1}$) is observed for all the cases.

Most previous studies consider only either impermeable biofilms or biofilms having a single-homogeneous permeability value. Our results show that the probability of finding very low velocities increases significantly when the biofilm is considered to be permeable. Figure 4a depicts $p(v)$ for all realizations of equivalent permeability fields within the biofilm used in this study (median: blue line; maximum deviation from the median: light blue shaded area). This provides us the variability in several metrics. For the higher velocities, which are highlighted by also plotting in semi-logarithmic scale (Figure 4b), there are no significant differences between the impermeable and homogeneous permeable biofilm, and neither between the different realizations. This is owing to the fact that most of the flow takes place in the preferential paths between the biofilm clusters. $p(v)$ for high velocities follows an exponential

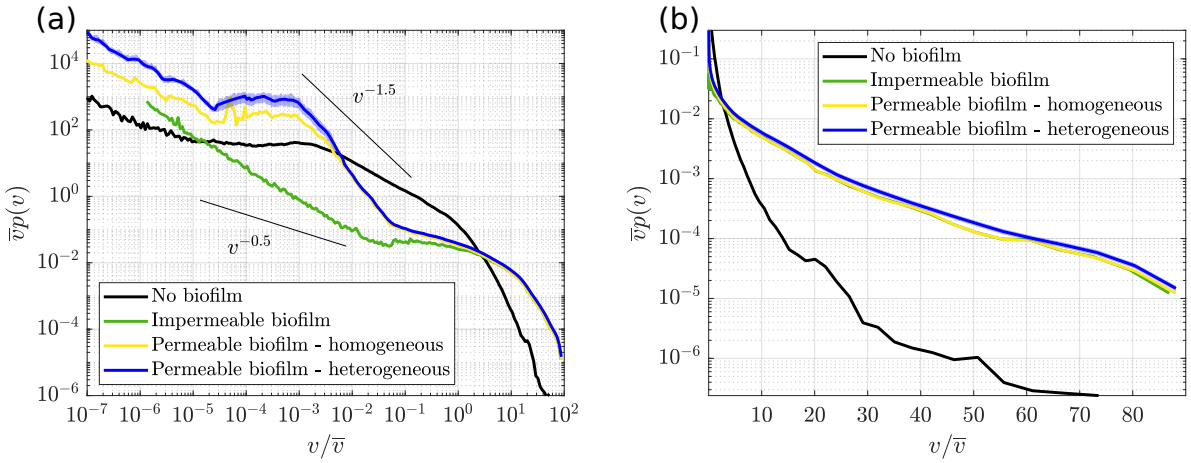


Figure 4: (a) Probability density function of fluid flow velocities $p(v)$ for the empty porous medium (black line), considering the biofilm impermeable (green line), considering the biofilm permeable (yellow line; single-homogeneous value, $\kappa_b = 5.12 \cdot 10^{-12}$ m$^2$), and for ten realizations of the biofilm permeability field, where the solid line (blue) indicates the median of all realizations and the shaded area represents the maximum deviation from the median for all realizations. (b) Same data plotted in a semi-logarithmic scale to highlight the exponential distribution of high velocities. The flow rate ($Q = 8.333 \cdot 10^{-8}$ m$^3$/s) is same for all.

trend ($\ln(p(v)) \propto -v$) in agreement with existing literature for unsaturated porous media but also for bioclogged porous media.[14,58,59] At intermediate velocities, just before the transition to very low velocities, larger deviations from the median are observed. These differences are reduced again at very low velocities. When comparing with previous experimental results from 3D particle tracking velocimetry (3D-PTV) measurements,[12] mainly high velocities are captured by the latter. This is due to the fact that the tracer particles used for 3D-PTV can not explore fluid flow velocities within the biofilm. Therefore, our approach allows to characterize the previously unseen shape of $p(v)$ at low velocities, i.e., the fluid flow velocities corresponding mainly to those within the biofilm.

## 3.2 Validation of the flow model with the tracer experiment

Figure 5 compares the normalized concentration (by the maximum concentration measured at the outlet, $c_{\max,\mathrm{KBr}}$) of KBr measured at the outlet (i.e., BTCs) in the tracer experiments (pulse injection) with the normalized concentration (by the maximum number of particles

collected at the outlet in a fixed time interval same as for the tracer test, $c_{\max,p}$) of simulated transport of particles (recirculated up to 10 times to mimic the total length of the reactor) for both the empty and the bioclogged porous medium. In the absence of biofilm (Figure 5a), an almost symmetrical BTC is observed. The transport of particles solved numerically performs well in general, although slight differences are observed. The first breakthrough is delayed, an earlier reduction in maximum concentration is seen, and a longer tail compared to the experimental data is observed. In the presence of biofilm (Figure 5b), and independent of whether the biofilm is impermeable (green line), homogeneous permeable (yellow line, see also Movie S1 in Supporting Information), or heterogeneous permeable (blue line), a much earlier first breakthrough and a more pronounced tailing of the tracer compared to the empty porous medium are observed. This is explained by the more marked preferential flow paths and low velocity and stagnation zones, similar to what is found in highly heterogeneous porous media.[60,61] This drives the so-called anomalous transport or non-Fickian solute dispersion. However, the numerically solved transport of particles for the impermeable (green line) and homogeneous permeable (yellow line) cases overestimate the arrival of mass at early times and underestimate the long tailing effect (i.e., the late arrival of mass) when compared with the tracer experiment. For the heterogeneous permeable case (blue line), a good agreement of the numerically solved transport of particles with the tracer experiment is observed. The initial rise and plateau of the normalized concentration are predicted well. The long tailing effect due to the presence of the heterogeneous biofilm is also well captured by the model, which, in very low permeability regions increases the residence time of particles (see Movie S2 in Supporting Information). The control of the heterogeneous permeability within the biofilm on transport becomes evident at very long times i.e., when diffusion becomes relevant (shaded area representing the maximum deviation from the median for all realizations). Note that tracer concentrations were already below the detection level in this experiment at these very long times. We believe our fluid flow simulations and the transport of particles, although developed from the imaged region (1/10 of the total reactor length), are representative of

the full reactor.

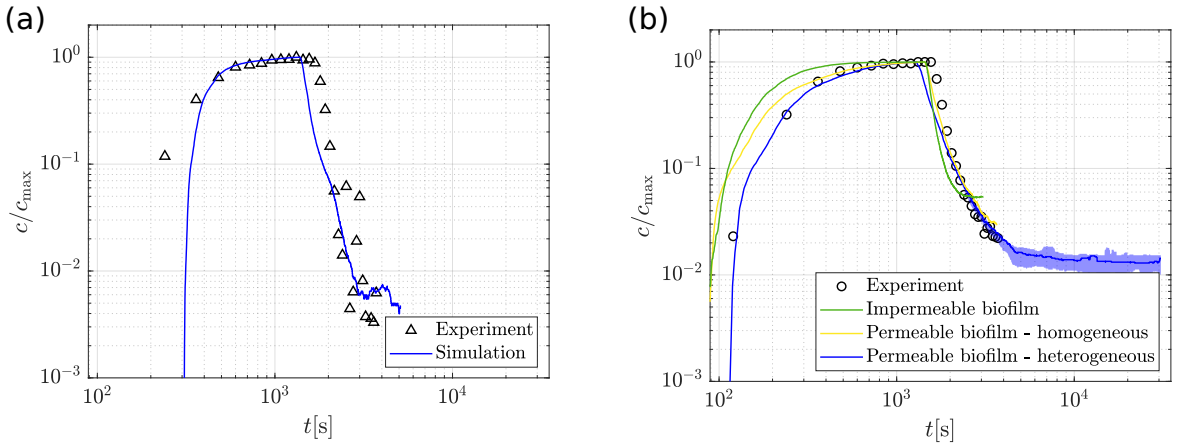


Figure 5: Comparison of the normalized breakthrough curves (BTCs) measured at the outlet for a pulse injection of KBr (symbols) and the simulated transport of particles-reinjection protocol for both (a) the empty porous medium (blue line) and (b) the bioclogged porous medium, including impermeable (green line), homogeneous permeable (yellow line) and heterogeneous permeable (blue line) biofilm. The blue line in panel (b) represents the median concentration for all biofilm permeability field realizations and the shaded area is the maximum deviation from the median.

## 3.3 Impact of the biofilm permeability heterogeneity on fluid mixing and reactions

To assess the control that the permeability heterogeneity within the biofilm exerts on the mixing of fluids and mixing-driven reactions, we first compute the mixing volume $V_{\mathrm{m}}$. Figure 6 shows the evolution of $V_{\mathrm{m}}$ with dimensionless time $t/t_a$. The smaller magnitude of $V_{\mathrm{m}}$ for the bioclogged porous medium cases at initial times, i.e., homogeneous (yellow line) and heterogeneous biofilm (blue line is the median for all biofilm permeability field realizations and the shaded area is the maximum deviation from the median), than in the absence of biofilm (black line) is occurring due to the reduced empty pore space. As the solute pulse invades the pore space, $V_{\mathrm{m}}$ rises rapidly following a non-Fickian almost ballistic behavior ($V_{\mathrm{m}} \sim t^1$) regardless of the case, as previously seen in unsaturated conditions in 2D and 3D.[62,63] At late times, the mixing shows a Fickian behavior, i.e., here diffusion is the mechanism controlling

mixing.[64,65] As compared to the empty porous medium, we see an earlier appearance of the Fickian regime ($V_{\mathrm{m}} \sim t^{0.5}$) when the biofilm is present. There are significant differences when a single-homogeneous or heterogeneous permeability field within the biofilm is considered. The internal heterogeneity in the biofilm allows both the almost ballistic (at early times) and the Fickian (at late times) regime to be reached earlier. Between the different permeability realizations, there are no considerable differences in the temporal evolution of $V_{\mathrm{m}}$.

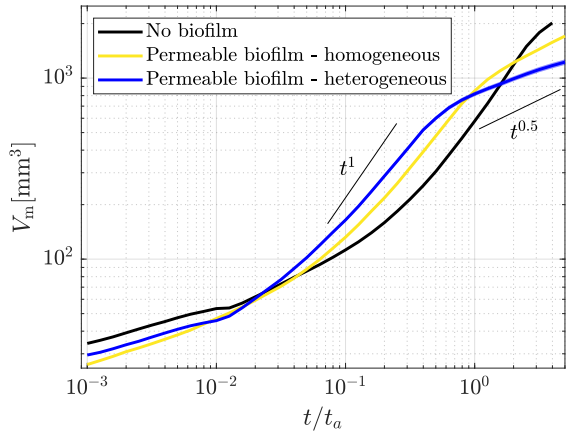


Figure 6: Mixing volume $V_{\mathrm{m}}$ as a function of dimensionless time $t/t_a$ for the empty porous medium (black line), considering the biofilm permeable (yellow line; single-homogeneous value, $\kappa_{\mathrm{b}} = 5.12 \cdot 10^{-12}$ m$^2$), and considering a heterogeneous permeability field within the biofilm (blue line, which represents the median of $V_{\mathrm{m}}$ for all biofilm permeability field realizations and the shaded area –visible only slightly at very late times– is the maximum deviation from the median).

Concentration gradients within the mixing volume control the local reaction rates. The global reaction rate $R$, computed as the integral of the local reaction rates, is impacted not only by the presence of the biofilm but also by its internal heterogeneity of it (Figure 7). In the presence of the biofilm (i.e., an immiscible and permeable phase within the pore space), $R$ initially increases in a similar manner as in the absence of biofilm, although with a higher magnitude. This is in stark contrast to the behavior seen for example in unsaturated porous media (i.e., containing an immiscible and impermeable phase within the pore space), where the reaction rate is enhanced at early times compared to fully saturated (so-called here empty) porous media.[52,62] For longer times ($t/t_a > 10^1$), when the chemical exits the

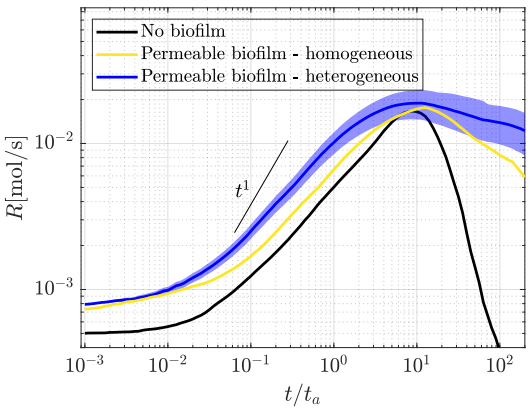


Figure 7: Temporal evolution of the global reaction rate $R$ for the empty porous medium (black line), considering the biofilm permeable (yellow line; single-homogeneous value, $\kappa_b = 5.12 \cdot 10^{-12}$ m$^2$), and the bioclogged porous medium (blue line, which represents the median of $R$ for all biofilm permeability field realizations and the shaded area is the maximum deviation from the median).

simulated region, a much slower drop off of $R$ with time for the bioclogged porous medium than in the empty porous medium is observed. While no significant differences in mixing volume between the different permeability field realizations are observed (Figure 6), there is a large variability, i.e., deviation from the median, for $R$. The permeability contrasts within the biofilm, i.e., fluid flow velocity contrasts, enhance the creation of concentration gradients (see Equation 4), in particular towards the very low permeability regions. Therefore, while differences in the permeability field within the biofilm do not impact the process of mixing significantly, they can control the reactivity in the system. This result differs from what has been observed in unsaturated porous media, where statistically equivalent organizations of the immiscible phase (e.g., air) do not impact mixing nor reaction.[37]

## 3.4 Chemical uptake rate with biofilm permeability heterogeneity

If the chemical injected as a pulse instead of reacting with the resident solution is taken up by the bacteria composing the biofilm, a depletion in concentration and therefore mass in the liquid phase occurs. Figure 8 shows the temporal evolution of the mass of dissolved chemical uptake by the biofilm $M_{\text{uptake}}$ for the homogeneous (yellow line) and the heterogeneous biofilm

(blue line is the median for all biofilm permeability field realizations and the shaded area is the maximum deviation from the median). Like the global reaction rate $R$, the uptake by the biofilm is impacted by the heterogeneity in the biofilm permeabilities. For both the homogeneous and heterogeneous cases, the uptake increases with dimensionless time as the chemical pulse are made available to the biofilm structures, although the homogeneous case has smaller uptake. As seen in Figure 6, the heterogeneous case mixes faster, and therefore more biofilm is exposed to the chemical. However, this results in a lower mean concentration in the solution (i.e., faster dilution) to be taken up by the bacteria composing the biofilm.

While chemical availability is usually considered the main limiting factor (i.e., consumption rates by bacteria are higher) in many applications,[66] we have demonstrated that not only the shape[54] and the spatial distribution[67] of the biofilm within the porous space have an impact on the biochemical reaction rates, but also the internal heterogeneity within the biofilm has to be considered when accurate predictions of bio-accumulation and bio-remediation, i.e., efficiency, are aimed for.

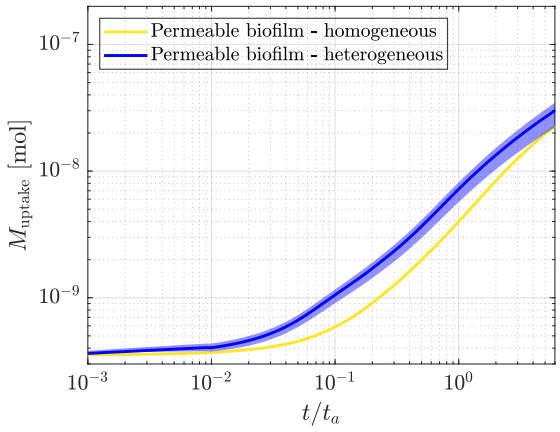


Figure 8: Temporal evolution of the mass of dissolved chemical accumulated in the biofilm $M_{\text{uptake}}$ for the homogeneous biofilm (yellow line) and for the heterogeneous biofilm (blue line, which represents the median of $M_{\text{uptake}}$ for all biofilm permeability field realizations and the shaded area is the maximum deviation from the median).

In this work, we have used X-ray images of a bio-clogged porous medium at the pore scale to generate equivalent heterogeneous permeability fields within the biofilm. Using a

numerical approach validated with experimental results, we have shown the impact of biofilm and of its internal heterogeneity on fluid flow velocities. The permeable and heterogeneous character of the biofilm, besides controlling intermediate velocities, alters the distribution of low velocities that deviate from those when the biofilm is impermeable. The latter is analogous to what has been observed for unsaturated (e.g., air) porous media.[58,59] The permeability heterogeneity of the biofilm does not impact significantly the mixing of fluids, however, the existence of low permeability regions within the biofilm enhances the formation of concentration gradients, controlling the overall reactivity within the system. When biologically driven reactions are considered (e.g., chemical uptake), similar trends are observed regarding the significant impact of biofilm permeability heterogeneity on reactivity. We generally conclude that it is important to consider permeability heterogeneity within the biofilm and the uncertainty that their stochastic realization can introduce in predictions of bio-accumulation and bio-remediation. Many questions remain open such as the control of transient conditions on the processes studied here, i.e., the impact of the spatio-temporal variation of biomass (interplay between the fluid flow and the biofilm growth), or the impact of the spatial variability of cell density and metabolic activity within the biofilm on chemical uptake.

# Acknowledgement

IM and JJ-M acknowledge the financial support from the Swiss National Science Foundation (SNF, grant Nr. 200021_178986). VLM acknowledges support from the U.S. National Science Foundation (NSF) (EAR-1847689) and the Engineering Research Center Program of NSF under Cooperative Agreement (EEC-1449501).

# Supporting Information Available

The following files are available as Supporting Information (SI).

- SupportingInformation.pdf: Distribution of biofilm along the reactor; random field generation by Fast Fourier Transform Moving Average method; correlation length analysis; protocol of particles recirculation

- Movie_S1.mp4: Particle tracking animation in the bioclogged porous medium considering homogeneous biofilm permeability.

- Movie_S2.mp4: Particle tracking animation in the bioclogged porous medium considering heterogeneous biofilm permeability.

# References


(1) O'Toole, G.; Kaplan, H. B.; Kolter, R. Biofilm formation as microbial development. *Annu. Rev. Microbiol.* **2000**, *54*, 49–79.

(2) Flemming, H.-C.; Wingender, J. The biofilm matrix. *Nat. Rev. Microbiol.* **2010**, *8*, 623–633.

(3) Fletcher, M. Bacterial biofilms and biofouling. *Curr. Opin. Biotechnol.* **1994**, *5*, 302–306.

(4) Flemming, H.-C. In *Marine and Industrial Biofouling*; Flemming, H.-C., Murthy, P. S., Venkatesan, R., Cooksey, K., Eds.; Springer Berlin Heidelberg, 2009; pp 3–12.

(5) Qureshi, N.; Annous, B. A.; Ezeji, T. C.; Karcher, P.; Maddox, I. S. Biofilm reactors for industrial bioconversion processes: Employing potential of enhanced reaction rates. *Microb. Cell Factories* **2005**, *4*, 24.

(6) Rittmann, B.; Nerenberg, R.; Lee, K.-C.; Najm, I.; Gillogly, T.; Lehman, G.; Adham, S. Hydrogen-based hollow-fiber membrane biofilm reactor (MBfR) for removing oxidized contaminants. *Water Supply* **2004**, *4*, 127–133.

(7) Boltz, J. P.; Morgenroth, E.; Sen, D. Mathematical modelling of biofilms and biofilm reactors for engineering design. *Water Sci. Technol.* **2010**, *62*, 1821–1836.

(8) Morgenroth, E.; Schroeder, E. D.; Chang, D. P.; Scow, K. M. Nutrient limitation in a compost biofilter degrading hexane. *J. Air Waste Manag. Assoc.* **1996**, *46*, 300–308.

(9) Kao, C.; Chen, S.; Liu, J. Development of a biobarrier for the remediation of PCE-contaminated aquifer. *Chemosphere* **2001**, *43*, 1071–1078.

(10) Kim, G.; Lee, S.; Kim, Y. Subsurface biobarrier formation by microorganism injection for contaminant plume control. *J. Biosci. Bioeng.* **2006**, *101*, 142–148.

(11) Pintelon, T. R.; Picioreanu, C.; van Loosdrecht, M. C.; Johns, M. L. The effect of biofilm permeability on bio-clogging of porous media. *Biotechnol. Bioeng.* **2012**, *109*, 1031–1042.

(12) Carrel, M.; Morales, V. L.; Beltran, M. A.; Derlon, N.; Kaufmann, R.; Morgenroth, E.; Holzner, M. Biofilms in 3D porous media: Delineating the influence of the pore network geometry, flow and mass transfer on biofilm development. *Water Res.* **2018**, *134*, 280–291.

(13) Orgogozo, L.; Golfier, F.; Buès, M. A.; Quintard, M.; Koné, T. A dual-porosity theory for solute transport in biofilm-coated porous media. *Adv. Water Resour.* **2013**, *62*, 266–279, A tribute to Stephen Whitaker.

(14) Carrel, M.; Morales, V. L.; Dentz, M.; Derlon, N.; Morgenroth, E.; Holzner, M. Pore-scale hydrodynamics in a progressively bioclogged three-dimensional porous medium: 3-D particle tracking experiments and stochastic transport modeling. *Water Resour. Res.* **2018**, *54*, 2183–2198.

(15) Bottero, S.; Storck, T.; Heimovaara, T. J.; van Loosdrecht, M. C.; Enzien, M. V.;

Picioreanu, C. Biofilm development and the dynamics of preferential flow paths in porous media. *Biofouling* **2013**, *29*, 1069–1086.

(16) Kurz, D. L.; Secchi, E.; Carrillo, F. J.; Bourg, I. C.; Stocker, R.; Jimenez-Martinez, J. Competition between growth and shear stress drives intermittency in preferential flow paths in porous medium biofilms. *Proc. Natl. Acad. Sci. U.S.A.* **2022**, *119*, e2122202119.

(17) Lewandowski, Z. Notes on biofilm porosity. *Water Res.* **2000**, *34*, 2620–2624.

(18) Beyenal, H.; Lewandowski, Z.; Harkin, G. Quantifying biofilm structure: Facts and fiction. *Biofouling* **2004**, *20*, 1–23.

(19) Stewart, P. S. Biophysics of biofilm infection. *Pathog. Dis.* **1994**, *70*, 212–218.

(20) Kurz, D. L.; Secchi, E.; Stocker, R.; Jimenez-Martinez, J. Morphogenesis of biofilms in porous media and control on hydrodynamics. *Submitted to Environ. Sci. Technol.* **2022**,

(21) Billings, N.; Birjiniuk, A.; Samad, T.; Doyle, P.; Ribbeck, K. Material properties of biofilms - A review of methods for understanding permeability and mechanics. *Reports on progress in physics. Physical Society (Great Britain)* **2015**, *78*, 036601.

(22) Wilking, J. N.; Zaburdaev, V.; Volder, M. D.; Losick, R.; Brenner, M. P.; Weitz, D. A. Liquid transport facilitated by channels in *Bacillus subtilis* biofilms. *Proc. Natl. Acad. Sci. U.S.A.* **2013**, *110*, 848–852.

(23) Deng, W.; Cardenas, M. B.; Kirk, M. F.; Altman, S. J.; Bennett, P. C. Effect of permeable biofilm on micro- and macro-scale flow and transport in bioclogged pores. *Environ. Sci. Technol.* **2013**, *47*, 11092–11098.

(24) Aufrecht, J. A.; Fowlkes, J. D.; Bible, A. N.; Morrell-Falvey, J.; Doktycz, M. J.; Retterer, S. T. Pore-scale hydrodynamics influence the spatial evolution of bacterial biofilms in a microfluidic porous network. *PloS one* **2019**, *14*, e0218316.

(25) Landa-Marbán, D.; Liu, N.; Pop, I. S.; Kumar, K.; Pettersson, P.; Bødtker, G.; Skauge, T.; Radu, F. A. A pore-scale model for permeable biofilm: Numerical simulations and laboratory experiments. *Transport Porous Med.* **2019**, *127*, 643–660.

(26) Karimifard, S.; Li, X.; Elowsky, C.; Li, Y. Modeling the impact of evolving biofilms on flow in porous media inside a microfluidic channel. *Water Res.* **2021**, *188*, 116536.

(27) Perez, L. J.; Parashar, R.; Plymale, A.; Scheibe, T. D. Contributions of biofilm-induced flow heterogeneities to solute retention and anomalous transport features in porous media. *Water Res.* **2022**, *209*, 117896.

(28) Seymour, J. D.; Gage, J. P.; Codd, S. L.; Gerlach, R. Anomalous fluid transport in porous media induced by biofilm growth. *Phys. Rev. Lett.* **2004**, *93*, 198103.

(29) Scheidweiler, D.; Peter, H.; Pramateftaki, P.; de Anna, P.; Battin, T. J. Unraveling the biophysical underpinnings to the success of multispecies biofilms in porous environments. *ISME J.* **2019**, *13*, 1700–1710.

(30) Beyenal, H.; Tanyolaç, A.; Lewandowski, Z. Measurement of local effective diffusivity in heterogeneous biofilms. *Water Sci. Technol.* **1998**, *38*, 171–178.

(31) Stewart, P. S. Diffusion in biofilms. *J. Bacteriol.* **2003**, *185*, 1485–1491.

(32) Kernan, C.; Chow, P. P.; Christianson, R. J.; Huang, J. Experimental and Computational Investigation of Biofilm Formation by Rhodopseudomonas palustris Growth under Two Metabolic Modes. *PloS one* **2015**, *10*, 1–18.

(33) Petroff, A. P.; Wu, T.-D.; Liang, B.; Mui, J.; Guerquin-Kern, J.-L.; Vali, H.; Rothman, D. H.; Bosak, T. Reaction–diffusion model of nutrient uptake in a biofilm: Theory and experiment. *J. Theor. Biol.* **2011**, *289*, 90–95.

(34) Davit, Y.; Byrne, H.; Osborne, J.; Pitt-Francis, J.; Gavaghan, D.; Quintard, M. Hydrodynamic dispersion within porous biofilms. *Phys. Rev. E* **2013**, *87*, 012718.

(35) Tyukhova, A. R.; Willmann, M. Connectivity metrics based on the path of smallest resistance. *Adv. Water Resour.* **2016**, *88*, 14–20.

(36) Di Dato, M.; Bellin, A.; Fiori, A. Convergent radial transport in three-dimensional heterogeneous aquifers: The impact of the hydraulic conductivity structure. *Adv. Water Resour.* **2019**, *131*, 103381.

(37) Jiménez-Martínez, J.; Alcolea, A.; Straubhaar, J. A.; Renard, P. Impact of phases distribution on mixing and reactions in unsaturated porous media. *Adv. Water Resour.* **2020**, *144*, 103697.

(38) Räss, L.; Kolyukhin, D.; Minakov, A. Efficient parallel random field generator for large 3-D geophysical problems. *Comput. Geosci.* **2019**, *131*, 158–169.

(39) Tran, N. H.; Chen, Z.; Rahman, S. S. Practical application of hybrid modelling to naturally fractured reservoirs. *Pet. Sci. Technol.* **2007**, *25*, 1263–1277.

(40) Carrel, M.; Beltran, M. A.; Morales, V. L.; Derlon, N.; Morgenroth, E.; Kaufmann, R.; Holzner, M. Biofilm imaging in porous media by laboratory X-Ray tomography: Combining a non-destructive contrast agent with propagation-based phase-contrast imaging tools. *PloS one* **2017**, *12*, 1–18.

(41) Mantoglou, A.; Wilson, J. L. The Turning Bands Method for simulation of random fields using line generation by a spectral method. *Water Resour. Res.* **1982**, *18*, 1379–1394.

(42) Shinozuka, M.; Jan, C.-M. Digital simulation of random processes and its applications. *J. Sound Vib.* **1972**, *25*, 111–128.

(43) Robin, M. J. L.; Gutjahr, A. L.; Sudicky, E. A.; Wilson, J. L. Cross-correlated random field generation with the direct Fourier Transform Method. *Water Resour. Res.* **1993**, *29*, 2385–2397.

(44) Oliver, D. S. Moving averages for Gaussian simulation in two and three dimensions. *Math. Geol.* **1995**, *27*.

(45) Ravalec, M. L.; Noetinger, B.; Hu, L. Y. The FFT Moving Average (FFT-MA) generator: An efficient numerical method for generating and conditioning Gaussian simulations. *Math. Geol.* **2000**, *32*.

(46) Durlofsky, L.; Brady, J. Analysis of the Brinkman equation as a model for flow in porous media. *Phys. Fluids* **1987**, *30*, 3329–3341.

(47) Ergun, S.; Orning, A. A. Fluid flow through randomly packed columns and fluidized beds. *IInd. Eng. Chem.* **1949**, *41*, 1179–1184.

(48) Ergun, S. Fluid flow through packed columns. *Chem. Eng. Prog.* **1952**, *48*, 89–94.

(49) Clift, R.; Grace, J.; Weber, M. *Bubbles, drops, and particles*; Dover Civil and Mechanical Engineering Series; Dover Publications, Incorporated, 2013.

(50) De Simoni, M.; Sanchez-Vila, X.; Carrera, J.; Saaltink, M. W. A mixing ratios-based formulation for multicomponent reactive transport. *Water Resour. Res.* **2007**, *43*.

(51) Willmann, M.; Carrera, J.; Sanchez-Vila, X.; Silva, O.; Dentz, M. Coupling of mass transfer and reactive transport for nonlinear reactions in heterogeneous media. *Water Resour. Res.* **2010**, *46*.

(52) Jiménez-Martínez, J.; Anna, P. d.; Tabuteau, H.; Turuban, R.; Borgne, T. L.; Méheust, Y. Pore-scale mechanisms for the enhancement of mixing in unsaturated

porous media and implications for chemical reactions. *Geophys. Res. Lett.* **2015**, *42*, 5316–5324.

(53) Hornung, R.; Grünberger, A.; Westerwalbesloh, C.; Kohlheyer, D.; Gompper, G.; Elgeti, J. Quantitative modelling of nutrient-limited growth of bacterial colonies in microfluidic cultivation. *J. R. Soc. Interface* **2018**, *15*, 20170713.

(54) Chaudhry, M. A. S.; Beg, S. A. A review on the mathematical modeling of biofilm processes: Advances in fundamentals of biofilm modeling. *Chem. Eng. Technol.* **1998**, *21*, 701–710.

(55) Holzner, M.; Morales, V. L.; Willmann, M.; Dentz, M. Intermittent Lagrangian velocities and accelerations in three-dimensional porous medium flow. *Phys. Rev. E* **2015**, *92*, 013015.

(56) Šimůnek, J.; van Genuchten, M. T. Modeling nonequilibrium flow and transport processes using HYDRUS. *Vadose Zone J.* **2008**, *7*, 782–797.

(57) Morales, V. L.; Dentz, M.; Willmann, M.; Holzner, M. Stochastic dynamics of intermittent pore-scale particle motion in three-dimensional porous media: Experiments and theory. *Geophys. Res. Lett.* **2017**, *44*, 9361–9371.

(58) Velásquez-Parra, A.; Aquino, T.; Willmann, M.; Méheust, Y.; Le Borgne, T.; Jiménez-Martínez, J. Sharp transition to strongly anomalous transport in unsaturated porous media. *Geophys. Res. Lett.* **2022**, *49*, e2021GL096280.

(59) Datta, S. S.; Chiang, H.; Ramakrishnan, T.; Weitz, D. A. Spatial fluctuations of fluid velocities in flow through a three-dimensional porous medium. *Phys. Rev. Lett.* **2013**, *111*, 064501.

(60) Yan, N.; Ji, Y.; Zhang, B.; Zheng, X.; Brusseau, M. L. Transport of GenX in saturated and unsaturated porous media. *Environ. Sci. Technol.* **2020**, *54*, 11876–11885.

(61) Aquino, T.; Aubeneau, A.; Bolster, D. Peak and tail scaling of breakthrough curves in hydrologic tracer tests. *Adv. Water Resour.* **2015**, *78*, 1–8.

(62) Markale, I.; Cimmarusti, G. M.; Britton, M. M.; Jiménez-Martínez, J. Phase saturation control on mixing-driven reactions in 3D porous media. *Environ. Sci. Technol.* **2021**, *55*, 8742–8752.

(63) Markale, I.; Velásquez-Parra, A.; Alcolea, A.; Jiménez-Martínez, J. Mixing controlled adsorption at the liquid-solid interfaces in unsaturated porous media. *Transport Porous Med.* **2022**, 1–17.

(64) de Anna, P.; Jiménez-Martínez, J.; Tabuteau, H.; Turuban, R.; Le Borgne, T.; Derrien, M.; Méheust, Y. Mixing and reaction kinetics in porous media: An experimental pore scale quantification. *Environ. Sci. Technol.* **2014**, *48*, 508–516.

(65) Le Borgne, T.; Dentz, M.; Bolster, D.; Carrera, J.; de Dreuzy, J.-R.; Davy, P. Non-Fickian mixing: Temporal evolution of the scalar dissipation rate in heterogeneous porous media. *Adv. Water Res.* **2010**, *33*, 1468–1475.

(66) Miller, E.; Menashe, O.; Dosoretz, C. G. A tailored permeable reactive bio-barrier for in situ groundwater remediation: removal of 3-chlorophenol as a case study. *Environ. Technol.* **2022**, *43*, 1200–1210.

(67) Yan, Z.; Liu, C.; Liu, Y.; Bailey, V. L. Multiscale investigation on biofilm distribution and its impact on macroscopic biogeochemical reaction rates. *Water Resour. Res.* **2017**, *53*, 8698–8714.